Chapter 1 Background

1.1 Introduction

SAE 1006 is a typical low carbon-manganese strip steel and is widely used in the automotive and other industries. In South Africa, Mittal Steel (SA), previously known as ISCOR, produces this steel at both its Vanderbijlpark (VDB) as well as at its Saldanha Steel (SS) plants. The former is a conventional strip producing plant using the Cold Charge Route (CCR) in which the slab from the continuous caster is allowed to cool to below the A_{r1} temperature before reheating for hot rolling. The Saldanha Steel plant, however, uses the Hot Charge Route (HCR) in a Compact Strip Plant where the continuously cast slab in the austenitic phase, enters the roller hearth reheating furnace (RHF) directly before hot rolling. The Compact Strip Production (CSP) plant has fewer rolling passes than the conventional plant at VDB with a slab thickness of 75 or 90 mm as opposed to 240 mm of the VDB plant.

After start up of the Saldanha Steel plant in 1998 it was soon found that the mechanical properties as well as the ease of recrystallisation after cold work, was different in nominally equivalent products produced at the respective two plants with the hot rolled strip produced at Saldanha Steel about 50 MPa higher in yield strength and decidedly more "sluggish" in recrystallisation after cold work than its counterpart produced at VDB. Apart from the difference in hot strip production processes, there was a difference in the chemical composition in the steels from these two plants, particularly with regards to sulphur content at the time. Both plants add calcium in their steelmaking process. However, at the time when this project was initiated, Saldanha

Chapter 1 Background

Steel used to add calcium to its liquid steel (calcium ladle treatment) and this resulted in relatively low sulphur content in these steels, i.e. typically less than 10 ppm. The discontinuation of the calcium ladle treatment later resulted in a slight increase in the sulphur content to more than 20 ppm. However this is still lower if compared to the equivalent VDB steel where the sulphur content is usually higher, even up to 100 ppm or more.

The nitrogen content in the steels from the two plants was not significantly different and ranged from 30 to 100 ppm with the latter high values resulting from Electric Arc Furnace melting. Unlike the sulphur content, both plants produced their hot rolled strip within the same carbon and manganese content range as these constituents were not process related.

The primary motivation for this study was the observation that was encountered by the users of these SAE 1006 Al-killed low carbon steels, i.e. the difference in the recrystallisation behaviour after cold work of the steels from the two respective plants, with the steel from Saldanha Steel exhibiting delayed recrystallisation after cold rolling. For customers to accommodate this problem, the continuous annealing (CA) lines had to be run slower (thus reducing productivity) and the batch annealing (BA) cycles required a higher annealing temperature (thus more energy input).

1.2 Previous work

Initial experimental work[1] that involved simulation of different coiling temperatures, the determination of hardnesses and

examination of carbide morphology, led to the preliminary conclusions that the delay in the recrystallisation of SS material was not a result of one single, obvious mechanism. It was suggested that the solute carbon and nitrogen might have contributed to the observed difference in the recrystallisation behaviour. However, the results were not conclusive in this regard as evidenced by the fact that even with lower "solute" nitrogen content, the SS material still exhibited sluggish recrystallisation behaviour. This led to the suggestion that a more comprehensive study on the influence of sulphur on the static recrystallisation of these steels after cold work should be pursued. The only tangible conclusion from this early study was that SS material that had been coiled experimentally at higher temperatures of 710°C and even above, now recrystallised rapidly, and this was considered as evidence of the role played by the precipitation of AlN prior to cold work and annealing of these steels. However, coiling at higher temperatures could not be implemented in practice due to the difficulty in the removal of scale from the coiled strip.

The results from hot rolling studies also indicated that the difference in the process routes, CCR versus HCR, would unlikely have a significant influence on the final austenite grain size of the hot strip at the finishing mill head (FMH)[2-4]. Despite SS material having a finer ferrite grain size, there was no significant difference in the work hardening behaviour of these two steels[1]. Hence, for the same amount of cold deformation, the amount of stored energy for recrystallisation would be almost the same for the two steels. Therefore, the emphasis of this study was placed on understanding the role played by chemical composition differences

rather than effects arising from differences in the respective process routes.

No comprehensive study to elucidate the factors that influence the kinetics of the recrystallisation behaviour of these two steels that were of nominally very similar chemical composition, with the exception of sulphur, had been done before. Therefore, the intention of this research project was to understand the cause of the difference in the recrystallisation behaviour of these steels and to suggest a remedy for the problem. Two groups of low carbon strip steels; one from Saldanha Steel with low to medium sulphur content, designated LS onwards, and the other from Vanderbijlpark with medium to high sulphur content, designated HS onwards, were obtained for this study.

Chapter 2 An overview of the processing of low carbon steel plate and hot strip

2.1 Introduction

Low carbon strip steels are steels with invariably low carbon, mostly below 0.1%, and with less than 1% total alloying additions. These steels are produced in sheet and strip form and they form a large share of the low carbon flat products steel market. Table 2.1 shows the typical chemical composition of these steels.

Table 2.1: Typical chemical composition of hot rolled low carbon steel sheet and strip[5].

Element [wt%]	C	Mn	S	P
Composition range	0.05 – 0.1	0.25 – 0.5	0.04 max	0.035 max

The manganese is added for solid solution strengthening and prevention of hot shortness through the precipitation of MnS instead of FeS formation. The production process of these low carbon steel flat-rolled products is summarised in a simplified flow chart in figure 2.1.

Low carbon steels have a wide range of yield strengths from 250 to 500 MPa. The different combinations of yield strength and ductility are achieved through a combination of adding alloying elements and thermomechanical processing. The latter involves reheating of the semi-finished products (slabs and ingots), the hot

rolling that finishes at a specific finishing temperature, controlled accelerated cooling on the run-out table that promotes the nucleation of a fine ferrite grain size from austenite and coiling at a specific temperature to achieve the desired mechanical properties.

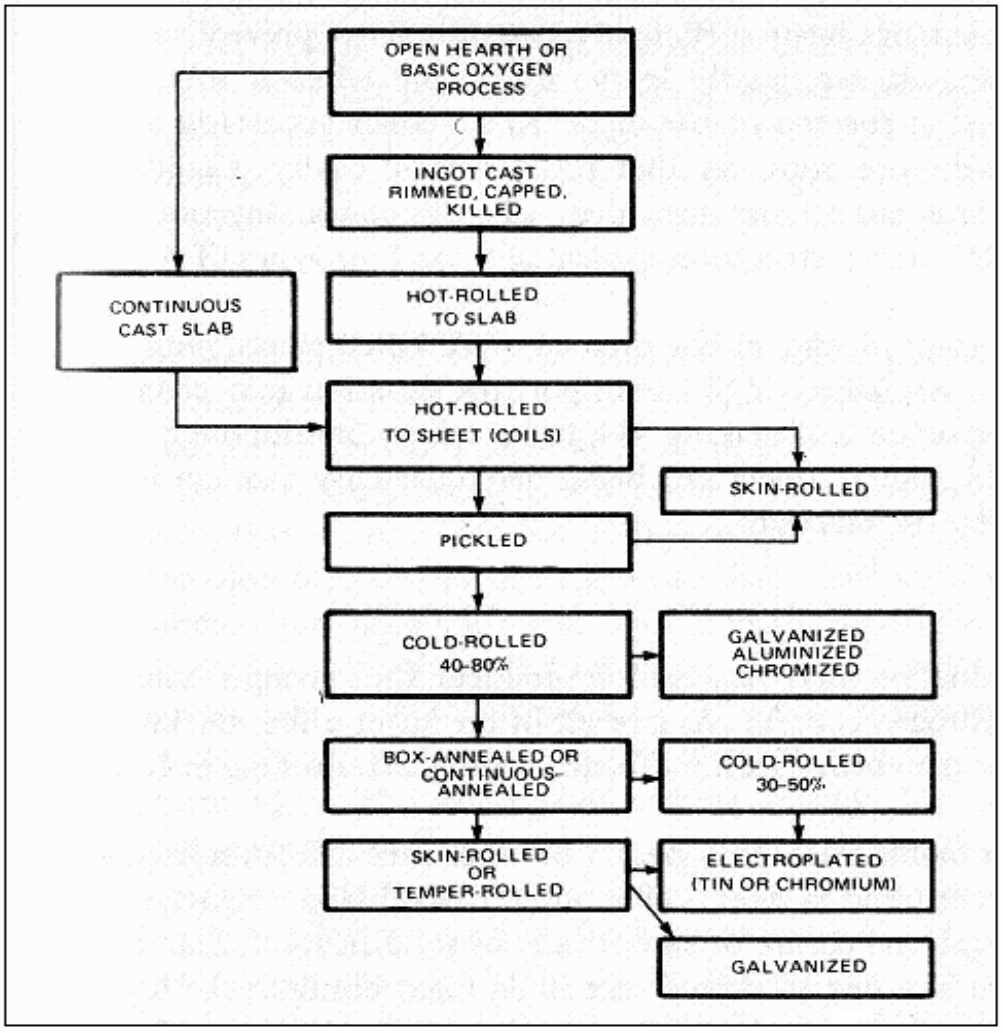

Figure 2.1: The simplified flow-chart for the production of low carbon strip steel[6].

Chapter 2 An overview of the processing of low carbon steel plate and hot strip

The low carbon content is essential for cold-formability requirements, as is also the low residual alloy content. In general, these low carbon strip steels can be divided into two categories[7]:

(i) Steels in which formability is of primary importance and strength is of lesser consequence. These steels are commonly used in car body pressings and similar applications.

(ii) Steels in which a higher strength is required and with a lesser cold-forming capability, such as the high-strength tin-plate steels where weight can be reduced by using thinner gauges.

2.2 Hot rolling of low carbon strip steel

There are mainly two types of hot strip mills namely, the Compact Strip Production (CSP) plants which usually employ the hot charge route (HCR) and the conventional strip production plants that use the cold charge route (CCR), see figure 2.2. The former are considered to be a more efficient way of producing steel vis-à-vis its design and the heat input. In the HCR process, after continuous casting, the slab is directly transferred to the reheat furnace for temperature equalization and while still in the austenite phase, is hot rolled. This is in contrast with the older conventional CCR processes where the continuous cast slab is allowed to cool from the austenite phase to room temperature to within the ferrite region and thereafter is reheated to the austenite phase and then hot rolled.

Chapter 2 An overview of the processing of low carbon steel plate and hot strip

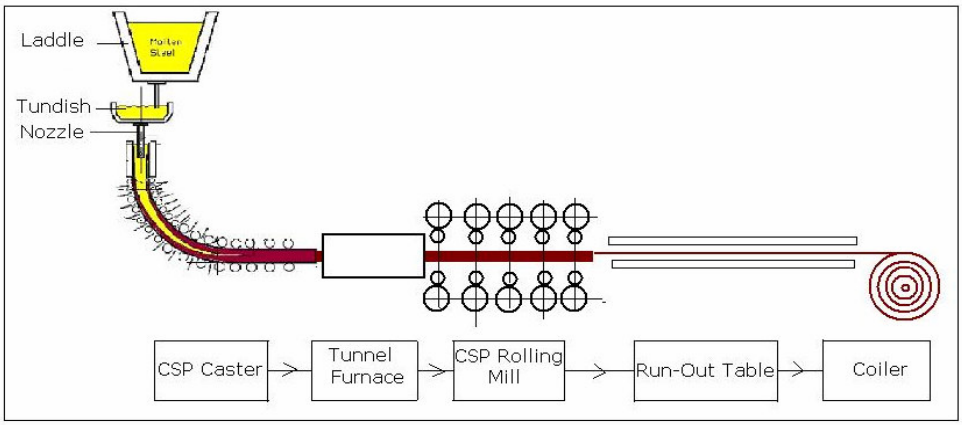

(a)

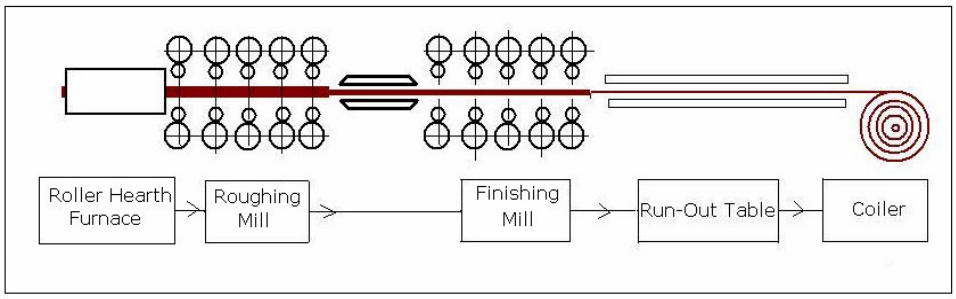

(b)

Figure 2.2: Hot strip rolling processes (a) the CSP and (b) the CCR.

Generally, most modern CSP plants are usually designed compactly with less hot rolling stages and they mostly start from thinner (typically 95 or 75 mm) continuously cast slabs compared to the conventional CCR where the slab thickness may typically be as large as 240 mm. The hot rolling process in a CSP is mostly characterised by higher pass strains, lower strain rates and longer interpass times. The longer interpass times and lower strain rates encourage dynamic and static recrystallisation during hot rolling. However this is off-set by the effect of the coarser as-cast starting

austenite grain size on recrystallisation and recovery during hot rolling. The starting austenite grain size in a CCR plant is generally smaller because of the prior austenite to ferrite phase change in the cast slab. However, these differences are smoothed out in the rolling process although some authors have observed finer final austenite grain sizes in CSP products that were attributed to the high pass strains in the last passes of the finishing mill[2-4].

Immediately after exiting the finishing mill, at temperatures mostly slightly above A_{r3}, the hot strip is sprayed with water on the run-out table in what is called accelerated cooling. The aim is to increase the driving force for the nucleation of ferrite from austenite. The resulting finer ferrite grain size improves both the yield strength and the toughness of these steels.

The hot strip is only cooled down to the coiling temperature which, for low carbon Al-killed strip steels, usually ranges between 580 and 650 °C. The coiling process is also an important stage in the production of these steels. The general practice is to ensure that the coiling temperature is not so high that excessive scaling or grain growth occurs nor too low that the steel is too stiff and "springy".

In aluminium treated steels, the coiling temperature and the cooling rate of the coil must be such that the AlN does not precipitate at this stage, because it is required to precipitate later during annealing after cold work in order to control the texture and subsequent cold formability of the strip. The precipitation of

Chapter 2 An overview of the processing of low carbon steel plate and hot strip

AlN during annealing after cold work promotes the nucleation of a preferred crystallographic texture ({111} texture in the plane of the sheet) that is necessary for deep drawing. The precipitation of AlN in these steels, therefore, performs a vital function and has been studied and reviewed extensively[8-11].

Aluminium is not only added to these low carbon steels for texture control alone but for other reasons which include deoxidation of the liquid steel, prevention of strain aging by nitrogen and also for grain refinement. In general, the aluminium content is kept within the range 0.02 to 0.05%Al.

3.1 Nucleation in solid solutions

The fundamental reason why a phase transformation takes place in a system is that the initial state is thermodynamically unstable relative to the final state i.e. the phase transformation allows the system to move to a lower free energy state. For phase transformations that take place at constant pressure and temperature the relative stability of the system is determined by its Gibbs free energy G where:

$$G = H - TS \tag{3.1}$$

where H is the enthalpy, T is the absolute temperature and S is the entropy of the system.

The free energy change ΔG between the initial and final state determines whether the reaction will proceed or not i.e. for the system to lower its free energy status, ΔG must be negative or alternatively $d\Delta G/dr$ must be negative for a still growing embryo. Therefore a necessary criterion for any phase transformation is:

$$\Delta G = G_2 - G_1 < 0 \tag{3.2}$$

where G_1 and G_2 are the free energies of the initial and final states respectively i.e.:

For a homogeneous nucleation and where the strain energy between the second phase and the host matrix is negligible, the free energy change ΔG can be presented mathematically by the

chemical driving force $(\frac{4}{3}(\pi r^3 \Delta G_v))$ and the retarding force $(4\pi r^2 \gamma_s)$, see figure 3.1. i.e.:

$$\Delta G = -\left(\frac{4}{3}(\pi r^3 \Delta G_v)\right) + 4\pi r^2 \gamma_s \qquad (3.3)$$

where r is the particle radius, γ_s is the interfacial energy and for an ideal solid solution, the chemical driving force $\triangle G_v$ is given by:

$$\Delta G_v = RT \ln K_s \qquad (3.4)$$

where K_s is the solubility product.

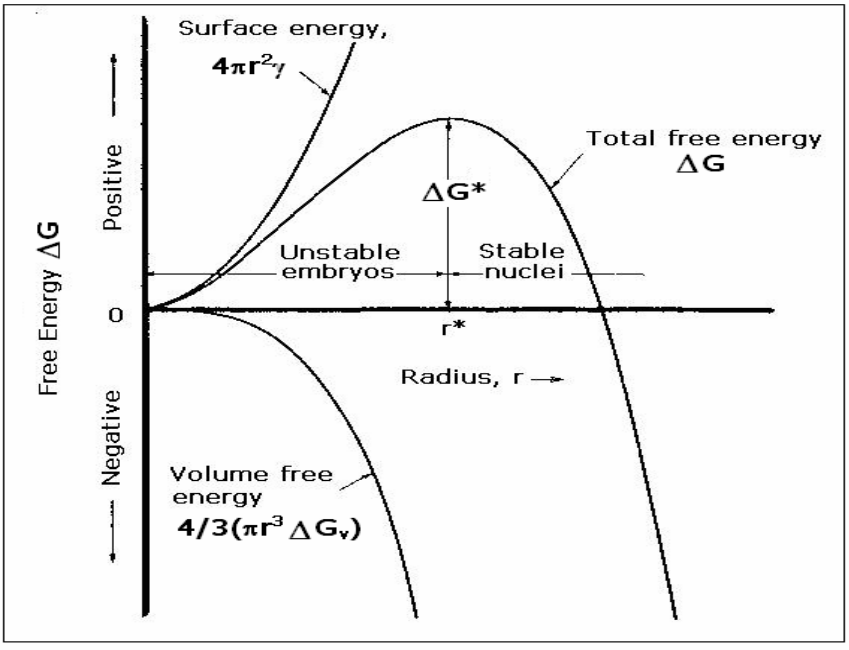

Figure 3.1: Free energy of formation of a stable nucleus where the retarding strain energy is very small

The activation energy ΔG^* and the critical embryo size r^* are given by equations 3.5 and 3.6:

$$r^* = \frac{-2\gamma_s}{\Delta G_v} \tag{3.5}$$

$$\Delta G^* = \frac{16\pi\gamma_s^3}{3(\Delta G_v)^2} \tag{3.6}$$

Any embryo that may form by statistical fluctuations in the matrix will grow only if the radius exceeds the critical size r^*. If it is smaller than r^* it can lower its free energy by re-dissolving into the matrix, figure 3.1.

At equilibrium the chemical driving force ΔG_v is given by:

$$\Delta G_v = \frac{\Delta H(T - T_e)}{T_e} = \frac{\Delta H \cdot \Delta T}{T_e} \tag{3.7}$$

A higher undercooling provides a greater chemical driving force for the phase change i.e. below the equilibrium temperature T_e the chemical driving force ΔG_v is negative and increases with undercooling. The values of the surface energy γ_s in equations 3.5 and 3.6 are generally assumed to be independent of temperature. Therefore, substituting for ΔG_v:

$$r^* = \frac{-2\gamma_s}{\Delta G_v} = -2\gamma_s\left(\frac{T_e}{\Delta H \Delta T}\right) \tag{3.8}$$

$$\Delta G^* = \frac{16\pi\gamma_s^3}{3(\Delta G_v)^2} = \frac{16\pi\gamma_s^3}{3}\left(\frac{T_e}{\Delta H \Delta T}\right)^2 \qquad (3.9)$$

The temperature dependence of r* and ΔG^* may, therefore, be assessed in terms of the temperature dependence of the chemical driving force ΔG_v i.e.:

$$r^* \propto \frac{1}{\Delta T}, \qquad \Delta G^* \propto \frac{1}{\Delta T^2} \qquad (3.10)$$

From equation 3.10, it may be seen that a higher undercooling results in smaller critical embryos and a smaller activation energy is required for the nucleation of those embryos. As a result, the nucleation rate would be higher and would generally lead to finer particles.

Precipitation of a particle from solid solution may cause some lattice strain because of differences in lattice spacing between the matrix and the particle or because of differences in densities between the two. Hence equation 3.3 then becomes:

$$\Delta G = \frac{4}{3}\pi r^3(\Delta G_v + \Delta G_\varepsilon) + 4\pi r^2 \gamma_s \qquad (3.11)$$

where ΔG_ε is the strain energy around the second phase and is a further retarding force.

The subject of strain energy ΔG_ε around a precipitate has been given attention by many authors[12-15]. The structural misfit δ due to differences in lattice spacing between the precipitate and the matrix is given by:

$$Misfit \quad \delta = \frac{\left(a_{ppt} - a_m\right)}{a_m} \tag{3.12}$$

where a_{ppt} and a_m are the lattice parameters for the precipitate and matrix respectively.

The magnitude of the strain is determined by a number of factors. The important ones are the disregistry, the elastic characteristics of the two phases, the nature of the strain and the shape of the particles. For a spherical particle with radius $(1+\delta)r_o$, the strain energy around a coherent particle is given by[12-14]:

$$\Delta G_{\varepsilon-coh} = \frac{6G_m V\delta^2}{\left[1+\frac{4G_m}{3K}\right]} \tag{3.13}$$

where G_m is the shear modulus, K is the bulk modulus and V is the volume of the particle $V = (4/3)\pi r^3$

and for incoherent particles[15]:

$$\Delta G_{\varepsilon-incoh} = 6G_m V\delta^2 f\left(\frac{c}{a}\right) \tag{3.14}$$

where f(c/a) depends on the shape of the particle through the dimensions a and c of a spheroid.

Since the strain energy ΔG_ε is positive (for both positive and negative δ misfit values) and the chemical driving force ΔG_v is negative, the result is that lattice strain increases both the activation energy ΔG^* and the critical r^* for the nucleation of the new phase, see equations 3.8, 3.9 and 3.11. The overall effect is that the nucleation rate $\dot{N}$ of the new phase may be significantly reduced or completely halted. Some authors[16-18] have modeled the effect of the strain energy ΔG_ε on the homogeneous nucleation parameters (critical radius r*, activation energy ΔG^* and nucleation rate $\dot{N}$) in a Cu-1at% Co alloy with a lattice misfit of 1.7% and their results are shown in figure 3.2.

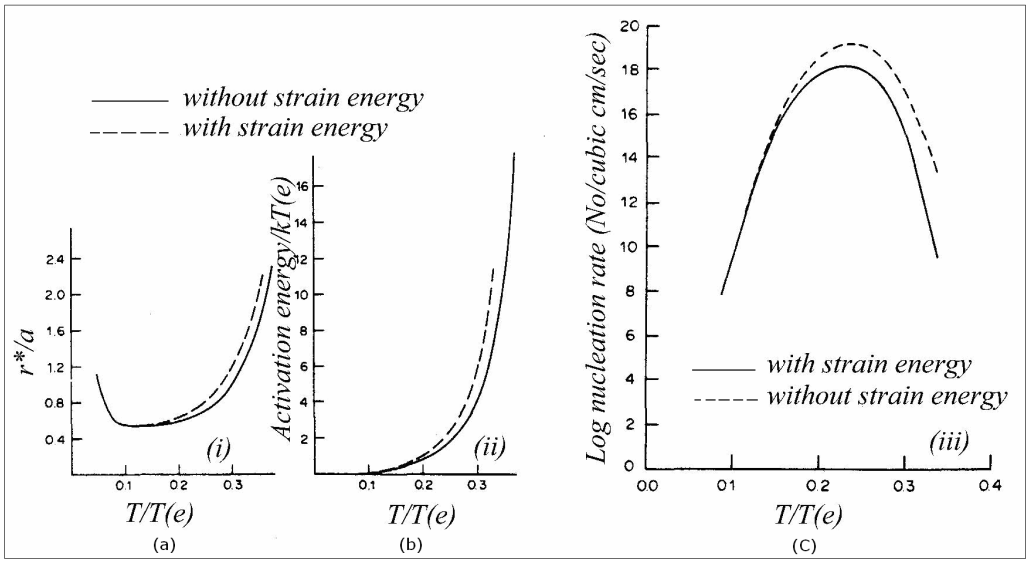

Figure 3.2: The effect of strain energy on the calculated nucleation parameters for the homogeneous nucleation of spherical Co precipitates in a Cu – 1at%Co alloy with a misfit of 1.7% between the

two phases. (a) The critical radius r* for nucleation normalised to the atomic radius a, (b) The activation energy ΔG* normalised to the temperature parameter kT_e and (c) the nucleation rate Ṅ. In all three cases these are shown as a function of the undercooled temperature T/T_e where T_e is the equilibrium solubility temperature[16].

The system may lower the strain energy around the particle by a number of ways, *inter alia* the formation of misfit dislocations, formation of ledges and kinks in the interface and eventually complete loss of coherence.

3.2 Heterogeneous nucleation in solid solutions

The nucleation of a second phase in solid solutions is a subject that has been given attention by many authors[16-26]. Nucleation of a second phase can either occur homogeneously or heterogeneously. Homogeneous nucleation occurs when embryos form as stable nuclei randomly in the matrix while heterogeneous nucleation occurs where embryos grow into stable nuclei on preferred sites such as dislocations, vacancies, grain boundaries, stacking faults, other precipitates and inclusions. These preferred nucleation sites lower the nucleation barriers by, generally, lowering the surface and strain retarding energies during nucleation of the second phase and, therefore, a smaller activation energy for nucleation would be required for heterogeneous nucleation than for homogeneous nucleation $\left(\Delta G^*_{hom} > \Delta G^*_{het}\right)$. Figure 3.3 is an illustration of the surface energy

balance for heterogeneous nucleation of a particle α on another particle β with both of them in the matrix M.

When nucleation takes place on an existing particle instead of nucleating homogeneously in the matrix, a certain surface area of the particle A_β is removed from the system. This provides an additional driving force for nucleation and, therefore, is a negative term in the basic energy equation for nucleation as illustrated through the surface energy balance in figure 3.3. Therefore, the free energy with heterogeneous nucleation on any surface is given by:

$$\Delta G_{het} = -V\left(\Delta G_v - \Delta G_\varepsilon\right) + A_\alpha \gamma_{M\alpha} + A_\beta(\gamma_{\alpha\beta} - \gamma_{M\beta}) \qquad (3.15)$$

where A_α and A_β are the interface areas between the matrix and the particle α and the two particles respectively.

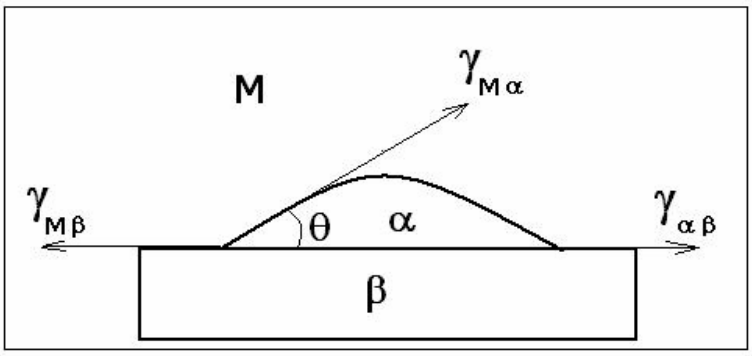

Figure 3.3: Heterogeneous nucleation of a particle α on another particle β in matrix M, where θ is the contact angle of the embryo α with the particle β, $\gamma_{\alpha\beta}$, $\gamma_{M\alpha}$ and $\gamma_{M\beta}$ are the surface energies on the particle α - particle β, particle α - matrix M and particle β - matrix M interfaces respectively.

Equation 3.15 indicates that the system will preferentially select those high energy sites first where it will gain the most energy through the additional driving force $A_\beta\gamma_{M\beta}$ for the nucleation of the second phase.

3.3 The nucleation rate of second phase

According to the classical theory of nucleation, the general time-dependent equation for the rate of homogeneous isothermal nucleation $\dot{N}$ is given by[27,28]:

$$\dot{N} = \frac{dN}{dt} = N_o Z \beta \exp\left(-\frac{\Delta G^*}{kT}\right)\exp\left(\frac{\tau}{t}\right) \qquad (3.16)$$

where N_o is the number of potential nucleation sites per unit volume, Z is the Zeldovich factor that accounts for the departure of the steady state from the equilibrium concentration of the critical nuclei, β is the frequency factor and is given by the number of atoms that reach the embryo per unit of time and is a function of the diffusion constant ($D = D_o\exp\{-Q/kT\}$), τ is the incubation time, k is the Boltzmann constant and N_o is the number of potential nucleation sites.

What equation 3.16 means is that if the incubation period τ is relatively large compared with the transformation time t, the transient nucleation will occupy a significant fraction of the whole isothermal transformation time. The ratio t/τ increases towards unity as the activation energy ΔG^* increases so that transient

effects are significant when nucleation is difficult. In the case of recrystallisation by the strain induced boundary migration mechanism, however, where pre-existing embryos (pre-existing recrystallisation interfaces) are involved, an "apparent" incubation time is believed to rather represent a time of slow growth or development of the pre-existing embryos to reach a critical size where more rapid growth is made thermodynamically possible.

If $t >> \tau$, equation 3.16 reduces to:

$$\dot{N} = \frac{dN}{dt} = N_o Z \beta \exp\left(-\frac{\Delta G^*}{kT}\right) \qquad (3.17)$$

The nucleation rate $\dot{N}$, which is the first derivative of the number of nuclei per unit volume versus time, is mostly not constant but decreases with the decrease in the driving force for nucleation from supersaturation as time progresses. In mathematical modelling, it is either assumed that all the nuclei form at a very early stage of transformation (i.e. site saturation) or are activated uniformly in time in the untransformed matrix (constant nucleation rate, $\dot{N}$).

3.4 Growth of precipitates from supersaturation

Once nucleation is practically complete (i.e. $\dot{N} = 0$), the particles continue to grow from the still supersaturated matrix at a rate controlled by the diffusion rate of the diffusing elements involved. This process is governed kinetically by the expression[29]:

$$r^2 - r_c^2 = 2D\Delta C\left(t - t_c\right) \tag{3.18}$$

where r_c and t_c are the particle radius and time when nucleation has ceased and all nuclei grow further only through diffusion of solute to the particle from the still supersaturated matrix, ΔC is the supersaturated concentration difference of solute between the particle surface and the surrounding matrix and D is the diffusion coefficient of the solute in the matrix.

3.5 Coarsening of precipitates

When growth of precipitates from supersaturation has ceased and the matrix has attained a quasi-equilibrium state, the system continues to lower its free energy through coarsening whereby the larger precipitates grow at the expense of the smaller ones. Unlike normal growth from supersaturation where the driving force is derived from the decrease in the chemical free energy ΔG_v, the driving force for coarsening is the decrease in the total surface energy $\gamma_s \Sigma A$ of the system as the smaller particles dissolve and the material is added to the larger ones. This process is modelled by the Lifshitz-Slyosov-Wagner [LSW] equation[30,31]:

$$\left(\bar{r}\right)^3 - \left(\bar{r_o}\right)^3 = \frac{8\gamma_s D C_e V_m^{\,2} t}{9RT} \tag{3.19}$$

where $\bar{r}_0$ is the mean particle size at time $t = 0$ and $\bar{r}$ is the mean particle size after time t, C_e is the equilibrium concentration of solute in the matrix, D is the diffusion

coefficient of the rate controlling diffusing species and V_m is the molar volume of the precipitate.

The rate at which the coarsening process takes place is practically always controlled in solid systems by the diffusion of the solute from the dissolving to the growing particles with the alternative interface control mechanism confined to only some liquid systems and a few very special solid systems.

3.6 Dissolution of precipitates above the solvus temperature

During dissolution of a precipitate there is no nucleation or dissolution barrier as in the case of precipitation. The precipitates have a finite non-zero initial radius R_o and decrease in size by mass transfer of the solute into the matrix behind the receding interface. Consequently, the resulting solute concentration profile is different from that obtained during growth, figure 3.4.

As is the case with coarsening, the particle dissolution process is mostly controlled by the diffusion of the detached solute into the matrix and in an infinite matrix, the dissolution velocity of the spherical precipitate is given by[32,33]:

$$\frac{dR}{dt} = k\left(\frac{D}{R} + \sqrt{\frac{D}{\pi t}}\right) \tag{3.20}$$

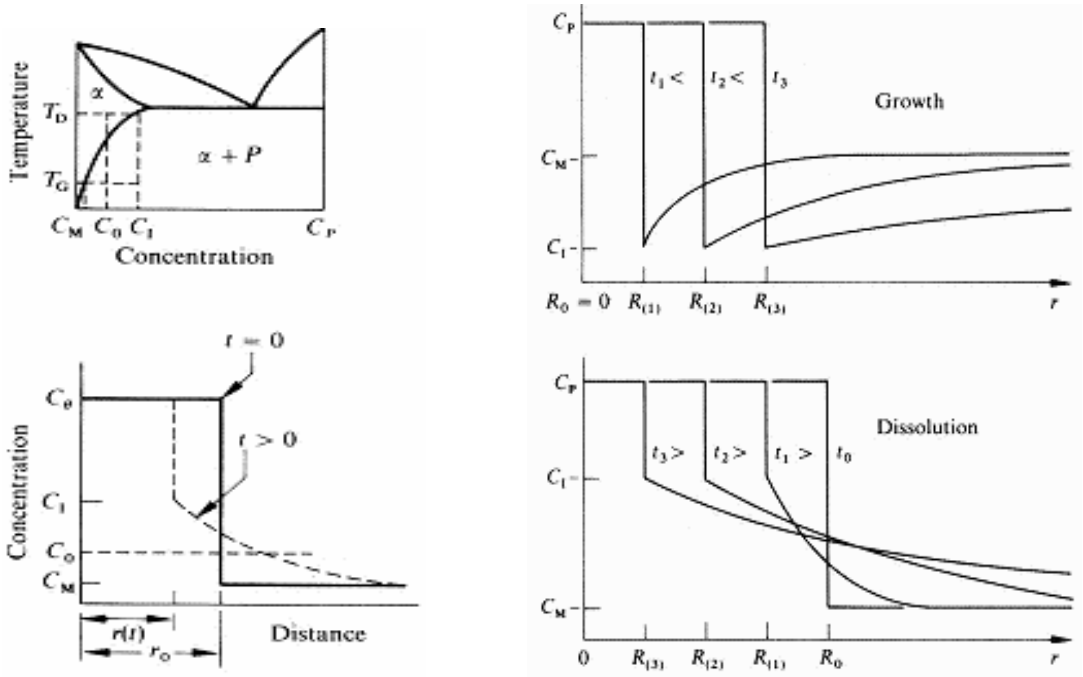

(a) (b)

Figure 3.4: (a) The solute concentration profiles around a dissolving precipitate which was initially in equilibrium with the solute depleted matrix and its corresponding binary phase diagram, (b) schematic comparison of the solute concentration profiles for precipitate growth and dissolution as a function of time[33].

where $$k = \frac{2(C_I - C_M)}{(C_P - C_I)} \qquad (3.21)$$

and where, as illustrated in figure 3.4, C_p is the composition of the precipitate and is considered constant with particle radius r and time t, C_I is the precipitate-matrix interface concentration, C_M is the equilibrium concentration in the matrix and D is the diffusion coefficient of the solute in the matrix.

The interface concentration, C_I, varies with the interface curvature and is governed by the Gibbs-Thompson equation which was modified by Hillert et al[32]:

$$C_{I(r)} = C_{I(\infty)} \exp\left[\frac{\gamma_p V_p}{RTC_p r}\right] \qquad (3.22)$$

where γ_p is the specific interfacial energy on the precipitate-matrix interface, V_p is the molar volume of the precipitate and C_p is the mole fraction of the solute in the precipitate.

Equation 3.20 is solved for R subject to the following boundary conditions[33,34]: $C_{(r=R,t)} = C_I \quad 0 < t \leq \infty$ and $C_{(r,\, t=0)} = C_M \quad r \geq R$.

Aaron et al[33] pointed out that since most alloys have a small supersaturation parameter, typically $|k| \approx 0.1$, i.e. $(C_p - C_M) >> (C_I - C_M)$, it is the concentration inequality $(C_p - C_M)$ rather than the interface reaction that controls the dissolution kinetics of precipitates in solid systems.